



# Defect-based analysis of the laser powder bed fusion process using X-ray data

Natan Nudelis<sup>1,2</sup> · Peter Mayr<sup>2</sup>

Received: 11 July 2022 / Accepted: 30 October 2022  
© The Author(s) 2022

## Abstract

Due to high production costs and a limited reproducibility of quality, the high potential of laser powder bed fusion (LPBF) has not been fully exploited yet. In fact, internal defects can have a detrimental effect on the fatigue behaviour and cause final component failure. Therefore, process-induced defects must be localized and evaluated at a higher level of detail. The present study deals with the correlation amongst pores and LPBF process parameters in AlSi10Mg components. Computed tomography (CT) allows an extensive examination of internal defects. Within this work, a total number of 2,939,830 pores detected in 96 cylindrical samples were analysed using CT. The formation of pores can be adjusted by varying the modified volume energy density, for example, by using various laser scanning speeds. Furthermore, the effect of powder preparation scan strategies (pre-heating and pre-sintering) on the formation of different pore types as well as the general reproducibility was examined. For instance, the shielding gas flow, contaminated protective windows of the lasers as well as prior powder preparation influence the formation of pores. Using prior laser powder preparation reduced the total number of pores at high scanning speeds up to 45%. When the scanning speed is increased, the number of spherical pores decreases and large and irregularly shaped pores appear. Interestingly, only the pre-heating process resulted in a reduced formation of spherical pores at low scanning speeds (1000 mm/s).

**Keywords** Laser powder bed fusion · AlSi10Mg · Computed tomography · Laser powder preparation strategies · Scanning speed study · Reproducibility

## 1 Introduction

By examining the pores in additive manufactured AlSi10Mg components, this study aims to provide answers about the correlation between process parameter and the resulting part quality. Additionally, internal defects can be utilized to evaluate an additive manufacturing system regarding reproducibility. Using various lasers or the intensity and direction of the shielding gas flow can have an impact on the resulting part quality. Therefore, amongst other influences, the location on the building platform plays an important role. On the other hand, the formation of pores is heavily dependent on the process conditions (e.g. powder, inert gas)

as well as the applied process parameters (e.g. laser power, hatch distance, layer thickness, laser scanning speed, various scanning strategies). The present research is focusing on AlSi10Mg components made by laser powder bed fusion (LPBF). According to the used material and additive manufacturing technology, three pore types (hydrogen-induced pores, keyhole pores and lack-of-fusion pores) are most frequently mentioned in the literature. These pore types can be distinguished by their shape, size and the cause of origin. Aboulkhair et al. [1] described gas-induced pores as spherically shaped and small in size (less than 100 µm in diameter). These pores preferably formed at slow laser scanning speeds from hydrogen trapped within the melt pool. The nucleation and growth of hydrogen-induced pores are highly dependent on the local hydrogen content, as well as the solubility difference between solid and liquid aluminium. The hydrogen solubility in solid pure aluminium is about a factor 10 lower than in the molten phase. Due to this fact, the hydrogen is going to enrich at the solidification front of the melt pool in gaseous form, if the hydrogen content is

✉ Natan Nudelis  
natan.nudelis@pro-fit.de

<sup>1</sup> FIT AG, Lupburg, Germany

<sup>2</sup> TUM School of Engineering and Design, Department of Mechanical Engineering, Technical University of Munich, Garching, Germany

higher than the solubility limit in the solid phase [2]. Furthermore, so-called keyhole pores exist, which are spherical in shape, but other than hydrogen-induced pores larger in diameter. Keyhole pores occur when the mechanism of melting is changing to so-called keyhole-mode laser beam melting, which is controlled by evaporation of metal due to a high power density of the laser beam [3]. The collapse of capillary cavities can finally leave pores in the root of the melt pool, usually filled with trapped gas which is used in the process chamber. Moreover, lack-of-fusion pores occur due to an insufficient laser energy input into the powder bed. On the one hand, this incomplete melting can be caused by weld spatter. The spatter is many times higher in volume and larger in diameter (between 200 and 500  $\mu\text{m}$ ) than the average powder particles [4]. Hence, those particles would need far more laser energy to be entirely melted, which is not provided by the process, and this leads to an unmolten gap without fusion. Furthermore, lack-of-fusion pores can occur due to the presence of oxide particles. Due to a residual amount of oxygen (0.1–0.2 vol%) in the processing chamber (usually filled with argon as inert or nitrogen as unreactive gas), an oxidation process starts on each of the scanned layers and also at the boundaries of the melt pool [5]. This results in a network of oxide layers, partly broken up during melting. Oxides can also influence the melting process and lead to lack of fusion. Independent from the cause of origin, all lack-of-fusion pores are irregularly shaped and large in diameter, partially filled with unmolten powder particles.

There are many process parameters that affect the pore formation and define the final component quality. Read et al. [6] observed that the laser power and scanning speed, as well as the interaction between the scanning speed and spacing, show the major influence on the porosity. The hatch distance controls the overlap amongst the scan tracks and has also an impact on the resulting porosity [7]. On the one hand, process parameters such as laser power, scanning speed, hatch distance or layer thickness can reduce the energy input into the powder bed and lead to incomplete melting and the formation of lack-of-fusion pores. On the other hand, e.g. slow scanning speeds result in hydrogen-induced pores due to trapped hydrogen within the melt pool [1], and a high laser power density will probably lead to an evaporation of metal and hence form keyhole pores [3].

Besides that, process strategies can affect the porosity. In order to reduce hydrogen-induced pores, pre-drying of the powder bed using a laser beam was carried out by Weingarten et al. [2]. They could show that the internal laser drying process reduces the pore density up to 90%. Many previous investigations focused on process optimisation of the LPBF process using AlSi10Mg [1, 5, 6, 8–10]. Due to the complexity of the LPBF process and the high amount of tuneable process parameters, strategies and conditions, the resulting quality is highly individual as well. The change of one or more

process parameters (e.g. laser power) or process conditions (e.g. powder quality) can result in a completely changed part quality. It seems to be obvious that precise investigations in more detail are necessary. In this framework, for a comprehensive understanding of the LPBF process and the resulting defects, a classification method using X-ray data was used based on a previous work of the authors [11].

X-ray computed tomography has already proven its ability as a useful tool to analyse defects in AlSi10Mg components [12–14]. On the other hand, Ortega et al. [15] mentioned undetected pores in Inconel 718 components due to X-ray penetration problems. It is important to mention that X-ray penetration problems can result in image quality issues and decrease the data quality [16]. When the component size is too big or the component material is too dense, the penetration of X-rays becomes an issue. These drawbacks can be overcome using higher voltage systems, beam filtration and optimized scanning parameters [16]. Furthermore, X-ray scans are incapable of examining pores smaller than the minimum voxel size, which is often mentioned as a criticism of CT in the context of porosity measurement [17, 18]. For instance, a typical minimum pore size needs at least three voxels wide to be accurately described. That means that a scan with a resolution of 10- $\mu\text{m}$  voxel size will quantify only pores > 30  $\mu\text{m}$  in diameter [16]. Large components and a low resolution lead to a loss of small pore data. Alternatively, various non-destructive techniques such as Archimedes method or ultrasonic method [19] are already applied. Nevertheless, X-ray computed tomography represents the most reliable non-destructive method of evaluating pore distributions [17]. Besides that, CT is used to inspect powder particles [20] or perform dimensional measurements by means of nominal-actual comparison [21].

The formation of specific defects as keyhole pores, hydrogen pores or lack-of-fusion pores depends on the induced volumetric energy density (*VED*) into the deposited metallic powder. The volumetric energy density is defined as the ratio between laser power  $P_L$  (W) and the product of layer thickness  $t$  (mm), laser scanning speed  $v$  (mm/s) and hatch spacing  $h$  (mm):

$$VED = \frac{P_L}{thv} [\text{J}/\text{mm}^3] \quad (1)$$

This *VED* equation is often named in literature (in [6, 8, 10]), but does not represent the energy input accurately enough. The common explanation of *VED* fails due to the non-observance of any material properties or interactions between the energy source and the powder bed. A modified version of the *VED* equation, which includes the material properties (absorption factor  $\beta$  and thermal diffusivity  $\alpha$ ) as well as the influence of the spot size diameter  $\varphi$ , was defined by Ferro et al. [22].

$$VED_{\text{modified}} = \frac{P_L \beta}{h \sqrt{4\alpha \varphi v}} [\text{J}/\text{mm}^3] \quad (2)$$

The absorption factor  $\beta$  is depending on the type of material which is melted. A powder bed has a much higher absorption factor than solid material. The reason for that is multiple reflections due to beam traps amongst the powder particles.

Internal defects seem to be an inevitable concomitant in the current state of laser powder bed fusion of Al alloys. Nevertheless, the knowledge about the formation and suppression of different pore types is an essential element in improving additive manufacturing applications. This work is intended to identify and evaluate important influences of process and environment on the quality of LPBF components. The presented results are supposed to show the wide range of analysis possibilities using CT data.

## 2 Methods

### 2.1 Manufacturing process, X-ray scan and VED calculation

For the X-ray scans, a cylindrical specimen shape was chosen (10 mm in diameter, 18 mm in height). The analysed

specimen was fabricated at FIT AG using a laser beam melting SLM500 machine (SLM Solutions, Lübeck, Germany), which is equipped with a Nd:YAG laser ( $\lambda = 1064 \text{ nm}$ ). The building direction was fixed vertically to the building platform. The maximum laser output is 400 W, whereby the output of the laser is usually set at 350 W. An overview of the process parameter settings for the production of the cylindrical specimens is given in Table 1. The chemical composition of the used AlSi10Mg powder is listed in Table 2.

The effect of scan strategies on the pore formation is analysed in the pre-heating and pre-sintering study. These two scanning strategies were performed to prepare the powder before the actual melting process in situ. The VED in the pre-heating process was  $0.3 \text{ J}/\text{mm}^3$  and for the pre-sintering  $0.5 \text{ J}/\text{mm}^3$ . The pre-heating of the powder with a lower laser power of 50 W and a spot size diameter of 0.25 mm is supposed to remove the moisture on the powder particles. The pre-sintering process of the powder ( $P_L = 50 \text{ W}$ ,  $\varphi = 0.08 \text{ mm}$ ) is supposed to stick the powder particles together, improve the heat transfer and stabilize the melt pool during the melting process. The standard scanning speed study analyses the influence of different scanning speeds without any prior preparation of the powder. In order to generate various volume energy densities (VEDs), the scanning speed was varied in 500 mm/s steps from 1000 to 2500 mm/s. The introduced VEDs from the laser beam

**Table 1** Overview of SLM500 process parameters for the fabricated cylindrical specimens

Parameter	Value	Used in following studies:
Laser power	350 W	Reproducibility, scanning speed
	50 W	Pre-sintering, pre-heating
Laser scanning speed	1150 mm/s	Reproducibility
	1000 mm/s	Scanning speed, pre-sintering, pre-heating
	1500 mm/s	Scanning speed, pre-sintering, pre-heating
	2000 mm/s	Scanning speed, pre-sintering, pre-heating
	2500 mm/s	Scanning speed, pre-sintering, pre-heating
Hatch spacing	0.17 mm	All
Spot size diameter	0.08 mm	Reproducibility, scanning speed, pre-sintering
	0.25 mm	Pre-heating
Layer thickness	50 $\mu\text{m}$	All

**Table 2** Chemical composition of the used AlSi10Mg powder (Tekna Advanced Material Inc., Sherbrooke, Canada)

Chemical composition in weight %													Used in following studies:
Cu	Fe	Mg	Mn	Ni	Zn	Pb	Sn	Ti	O	N	Si	H	
ICP-MS (ASTM E1479)									LECO (ASTM E1409)		ICP-OES (ASTM E1479)	LECO (ASTM E1447)	
<0.001	0.09	0.29	0.005	0.002	0.002	0.001	<0.001	0.03	0.032	<0.002	9.5	<0.002	Reproducibility
<0.001	0.13	0.25	0.005	0.004	0.002	0.001	<0.001	0.012	0.03	<0.002	9.62	0.002	Scanning speed, pre-sintering, pre-heating

into the deposited AlSi10Mg powder start at  $2.1 \text{ J/mm}^3$  (at  $1000 \text{ mm/s}$ ) and rise to  $2.4 \text{ J/mm}^3$  (at  $1500 \text{ mm/s}$ ),  $2.8 \text{ J/mm}^3$  (at  $2000 \text{ mm/s}$ ) and  $3.4 \text{ J/mm}^3$  (at  $2500 \text{ mm/s}$ ). All specimen variations for these studies were fabricated and CT-scanned three times (in total 36 cylindrical samples and 1,008,487 evaluated pores). Finally, 1,931,343 pores in 60 cylindrical samples were examined to check the reproducibility as well as the influence of different lasers and the shielding gas flow on the pore formation. The building platform of a SLM 500 machine has a building area of  $500 \text{ mm} \times 280 \text{ mm}$ . This building area was divided into 12 equal subareas each  $125 \text{ mm} \times 93.3 \text{ mm}$ . On each subarea, five cylindrical samples were fabricated, scanned and evaluated. The SLM 500 machine is equipped with four lasers. Each laser has its own working area, which can also overlap with other laser zones. It is worth mentioning that none of the specimen was built in a laser overlap zone. In order to calculate the modified *VED*, additional values are needed. Gu et al. [23] calculated the laser absorptivity along the beam path of AlSi10Mg powder in a range from 0.19 to 0.32. Within the scope of this work, the mean value of the calculated range ( $\beta = 0.255$ ) was used. The thermal diffusivity for AlSi10Mg about  $75 \text{ mm}^2/\text{s}$  (measured for a temperature of  $300 \text{ }^\circ\text{C}$ ) is taken from Yang et al. [24]. The X-ray scans were made using the Diondo d2 microfocuss CT system (Hattingen, Germany), which has a minimum voxel size of  $9.659 \text{ }\mu\text{m}^3$ . It is important to emphasize that a typical minimum pore size needs at least three voxels to be accurately described [16]. That means that scans with a resolution of  $9.659 \text{ }\mu\text{m}$  can only represent pores approx.  $> 30 \text{ }\mu\text{m}$  in diameter. Pores smaller than  $30 \text{ }\mu\text{m}$  are not visible in this work. Each of the scans was carried out in 1500 projections in a  $360^\circ$  sample rotation (1.4-s integration time per projection) using a power output of 9.5 W and a voltage of 190 kV. The reconstruction of raw CT data into a 3D model was performed with VGSTUDIO MAX 3.1.0 64 (Volume Graphics, Heidelberg, Germany). The analysed region of interest (ROI) includes a volume of  $785.4 \text{ mm}^3$ . The porosity within the ROI was analysed by using the VGDefx algorithm (Volume Graphics, Heidelberg, Germany).

## 2.2 Pore evaluation using computed tomography data

On the one hand, the fundamentals of the formation of pore types are already well understood. These internal defects can be seen as an individual process fingerprint, which contains a lot of information about the process conditions. On the other hand, X-ray pore evaluation methods have already been developed, which allow to classify pores accurately enough to exploit this individual information. The utilized classification method is taken from a previous work of the authors [11] and classifies the pore shape only in spherical and irregular shapes using three shape indicators ( $\Psi$ ,  $\Omega$  and *BB* factor). The first shape indicator

is the sphericity, which is defined as the ratio of surface area of a sphere with the same volume as the given pore to the pore's surface area.

$$\Psi = \frac{\pi^{\frac{1}{3}}(6 \times V_{\text{pore}})^{\frac{2}{3}}}{A_{\text{pore}}} \quad (3)$$

where  $V_{\text{pore}}$  is the pore volume and  $A_{\text{pore}}$  is the pore's surface area. The second shape indicator is the compactness of the pore and is expressed as the ratio of pore volume to the volume of a sphere, which is defined by the maximum diameter/radius around the pore.

$$\Omega = \frac{V_{\text{pore}}}{\frac{4}{3} \times \pi \times R_{\text{pore}}^3} \quad (4)$$

where  $R_{\text{pore}}$  is the maximum pore radius. Additionally, the bounding box dimensions can be used to classify a pore shape. On this account, three-dimensional descriptors *S*, *M* and *L* must be introduced, where *S* is the shortest pore dimension, *L* is the longest pore dimension and *M* describes the medium-sized pore dimension. Hence, the bounding box factor (*BB* factor) has been defined as follows:

$$BB - \text{factor} = \frac{S}{L} \quad (5)$$

The *BB* factor allows categorizing the pores into spherical or non-spherical shapes. An irregularly shaped geometry can fit in all bounding box aspect ratios, but a spherical pore can only fit in an almost perfect bounding box aspect ratio of 1:1:1. Due to this fact, the *BB* factor proved to be an appropriate indicator for this classification. All three shape indicators (sphericity, compactness and *BB* factor) were used to sort the pores in spherical or non-spherical. The classification criteria are shown in Table 3. The pores are divided into six classes (A–F), where classes A–C describe spherically shaped pores and D–F irregularly shaped pores. Combined with the information about the pore size, the classification of pore types such as hydrogen-induced pores, keyhole pores and lack-of-fusion pores is possible. The pore size is described by the maximum pore diameter of a sphere around the pore. Illustrations of possible pore shapes (classes A–F) are shown in Fig. 1.

## 3 Results and discussion

### 3.1 Influence of scanning speed and scanning strategies on the pore formation

The pore classification was used to observe the effects of varying laser scanning speeds including prior powder preparation scanning strategies, especially pre-sintering

**Table 3** Pore classification criteria using X-ray data [11]

Pore class	Diameter	Compactness	Sphericity	BB factor
Spherical	A $D_{pore} \leq 100 \mu\text{m}$	$\Omega \geq 0.4$	$\Psi \geq 0.6$	$BBF \geq 0.6$
	B $100 \mu\text{m} < D_{pore} \leq 200 \mu\text{m}$			
	C $D_{pore} > 200 \mu\text{m}$			
Irregular shaped	D $D_{pore} \leq 100 \mu\text{m}$	$\Omega < 0.4$	$\Psi < 0.6$	$BBF = [0,1]$
	E $100 \mu\text{m} < D_{pore} \leq 200 \mu\text{m}$			
	F $D_{pore} > 200 \mu\text{m}$			

and pre-heating. The used process parameters are listed in Table 1. Figure 2 illustrates the formed pore classes (mean values including the standard deviations) depending on the VED for the scanning speed parameters without any prior powder preparation. The higher the introduced energy into the powder bed, the fewer irregularly shaped pores (classes D–F) and more spherically shaped pores (classes A–C) occur. Pore classes E and F represent weak spots in an AM part and should be reduced by adapted process parameters or post-processing such as hot isostatic pressing. In addition to the melting process with the here called scanning speed parameters, pre-sintering and pre-heating scanning strategies were carried out before melting (see Table 1). These two scanning strategies were performed to prepare the powder before melting (more details in Section 2.1). The results of the parameter study using the pore classification are shown in Fig. 3 (mean values including the standard deviations).

First, the results of the scanning speed parameters without prior powder preparation were considered. When the scanning speed is increased, the number of spherically shaped pores (classes A–C, likely hydrogen and keyhole pores) decreases. On the other hand, the irregularly shaped porosity

(classes D–F, likely lack-of-fusion pores) increased. The total amount of pores at a scanning speed of 1000 mm/s was 36,256 pores. At 1500 mm/s, the porosity drops to 23,532 pores and increased again with rising scanning speed. In general, the prior pre-heating and pre-sintering process seems to stop the formation of pores with increasing scanning speed. A reason for that could be a stabilized melt pool due to an improved heat transfer through the formed powder cake (pre-sintering), as well as less moisture on the surface of the powder particles (pre-heating and pre-sintering). Interestingly, the pre-heating process seems to reduce the surface moisture on the powder particles and hence decreases the amount of spherically shaped hydrogen-induced pores (likely classes A and B) at scanning speeds of 1000 mm/s drastically. Weingarten et al. [2] also observed more hydrogen-induced pores at lower scanning speeds, as well as a reduction of these pores using laser drying. The total amount of pores at 1000 mm/s remains the same for all scanning strategies. Nevertheless, the pre-heating strategy leads to an increase of irregularly shaped pores instead of spherical pores. It is worth mentioning that irregularly shaped pores (commonly classes E and F) dictate the occurring component failure, most often by a single dominating crack propagation. Du

**Fig. 1** Illustration of pore classes A–F

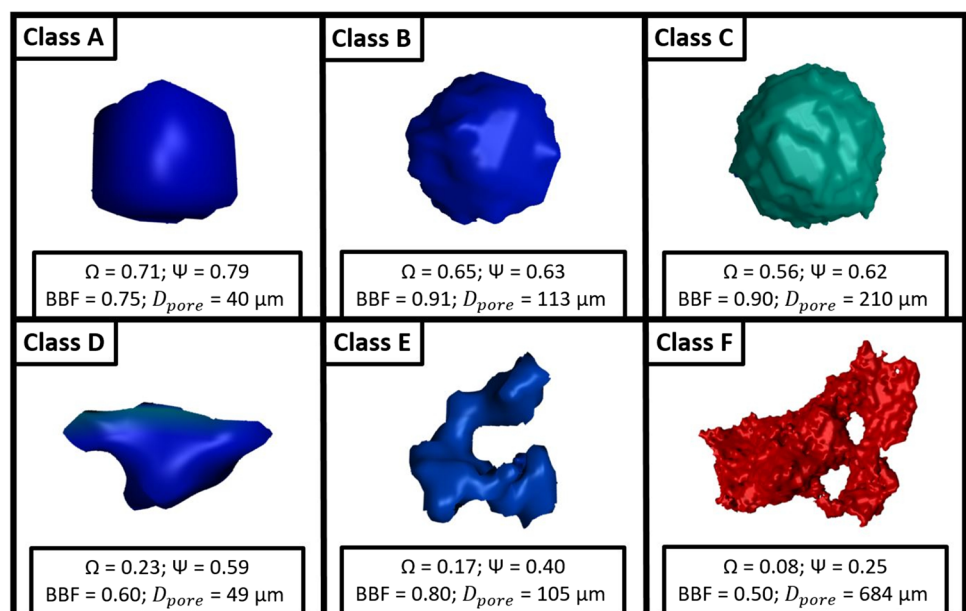
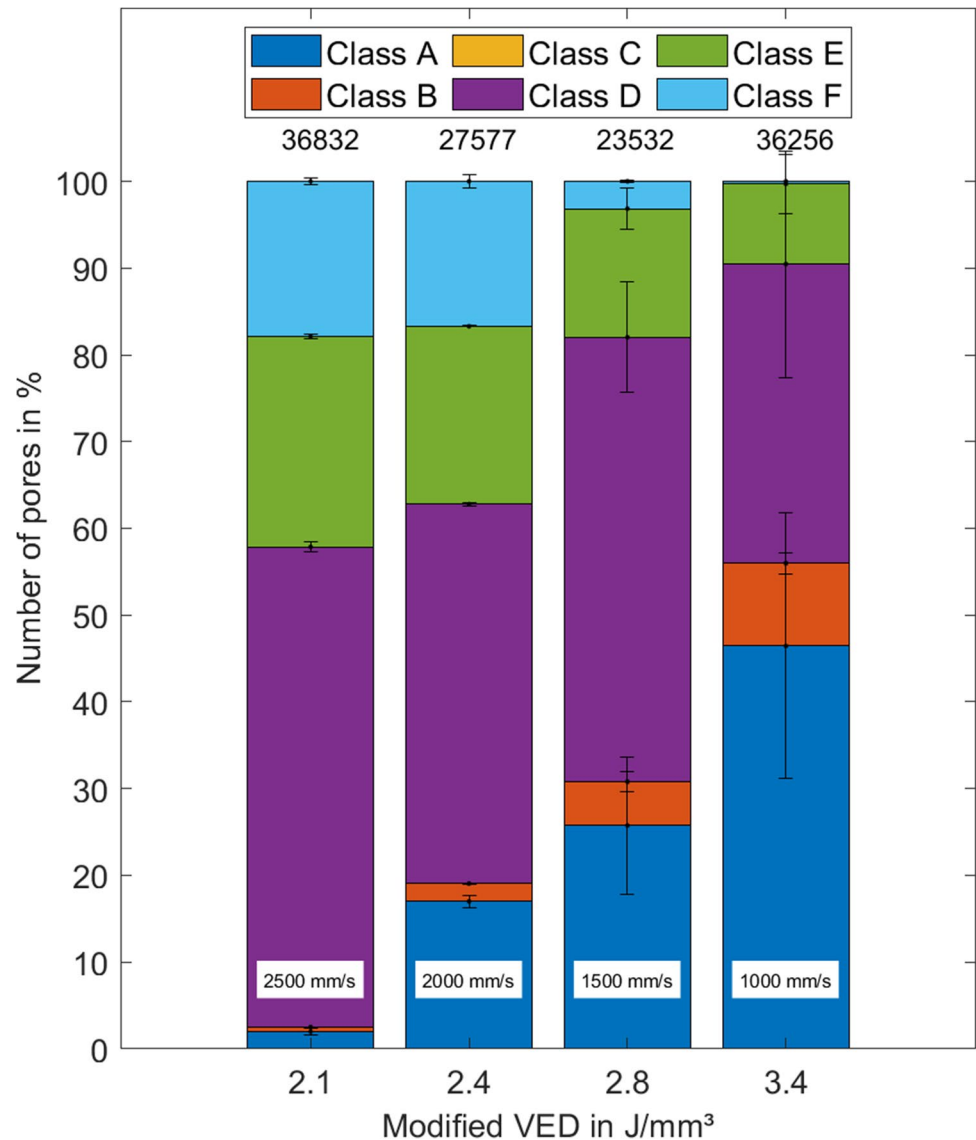


**Fig. 2** Pore classification depending on the modified *VED* for the scanning speed parameter settings without prior powder preparation



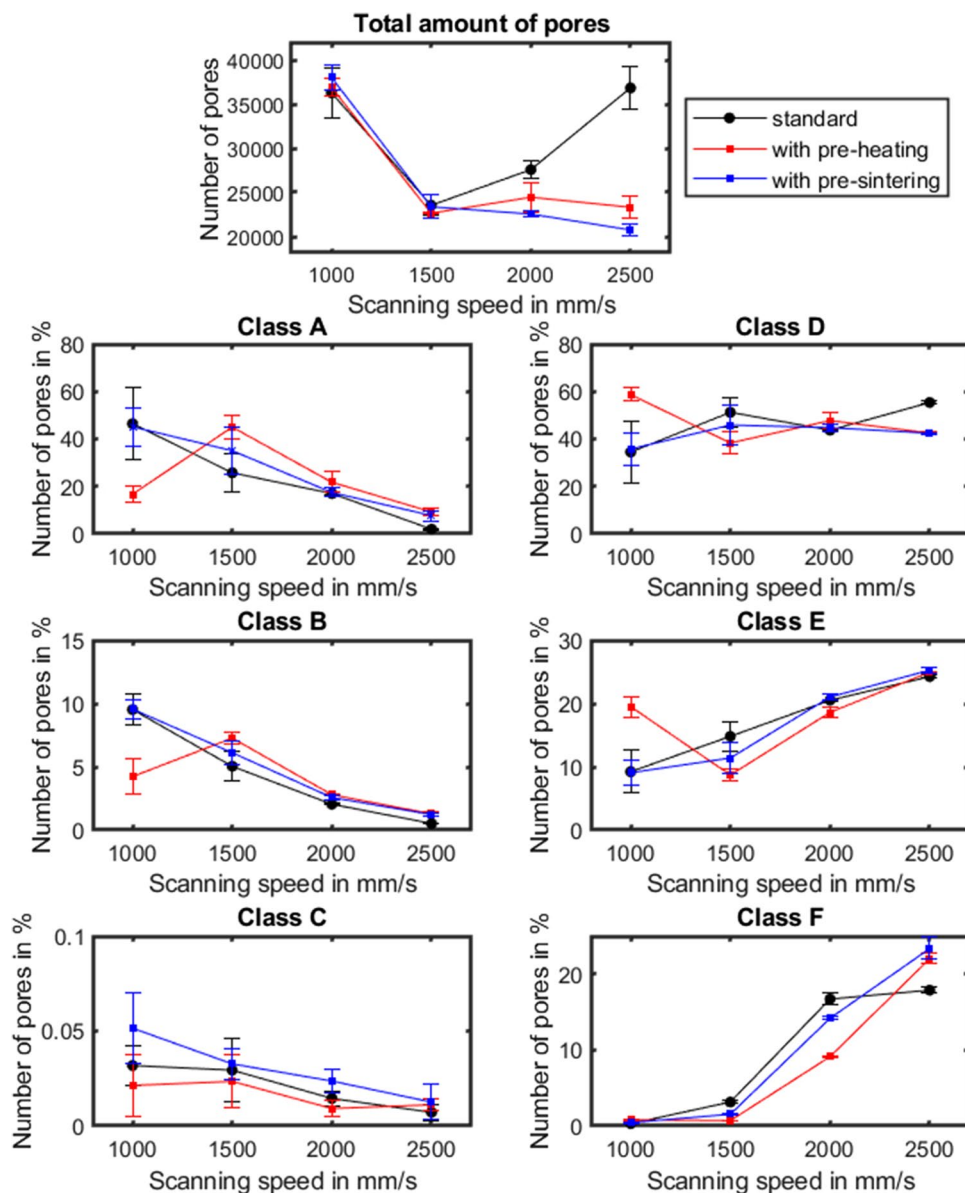
Plessis et al. [25] hypothesized that the largest pore is the origin of failure. Additionally, in a previous work of the authors [11], the effect of pore shape on emerging stress concentrations was analysed by means of FEA. The results show that stress concentrations are heavily dependent on pore shape and load direction. On the one hand, the highest stress concentrations appeared at pores with the largest cross-sectional transition, which is why nearly all irregularly shaped pores are a potential risk. On the other hand, spherical pores do not have any cross-sectional transition, which can cause high-stress concentrations. In this context, the pre-sintering process shows a reduced number of pores at higher scanning speeds, as well as an unchanged amount of spherically shaped pores at 1000 mm/s in comparison to the pre-heating strategy and the melting without prior powder preparation. The findings demonstrate that the modified *VED* can be used as an indicator for the formation of

different pore types and might serve as an appropriate tool for process adjustments. The pore classification using CT data allows detailed insights into the formation and suppression of pores using different parameter settings. Even if the formation of pores cannot be completely suppressed, investigations using CT-based analyses can contribute in finding the optimal process settings for individual applications.

### 3.2 Reproducibility study

Additionally, the presented classification method allows to evaluate a running manufacturing system and provides accurate information about its process conditions. For this reason, the pore classification method was used to check the reproducibility of LPBF parts. Furthermore, the influence of different lasers as well as the effect of the shielding gas flow on the formation of pores was investigated.

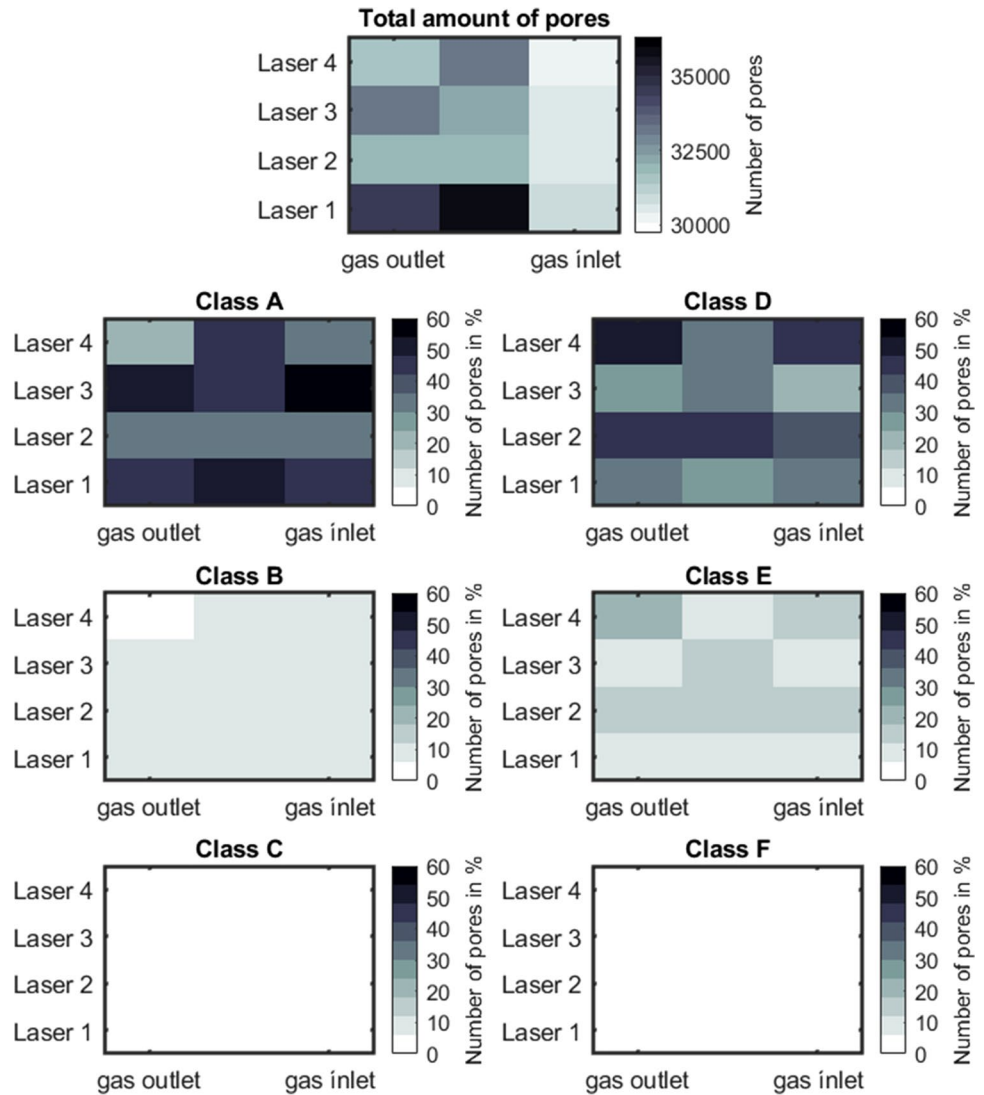
**Fig. 3** Pore classification results for various laser scanning speeds (1000–2500 mm/s) and prior scanning strategies (pre-heating, pre-sintering)



The used process parameters (reproducibility settings) are shown in Table 1. The results of this study, especially the total amount of pores, as well as the number of individual pore classes are visualized in Fig. 4. Some noticeable effects on the formation of pores could be observed. In contrast to the gas inlet side, the gas outlet side shows a much higher amount of porosity. Interestingly, the number of lack-of-fusion pores (classes D and E) is higher at the gas outlet side, compared to the gas inlet side. Obviously, weld spatter is responsible for the formation of lack-of-fusion pores at the gas outlet side. An instable melt pool can cause a high amount of weld spatter, which are many times higher in volume and larger in diameter than the average powder particles [4]. The weld spatter is deflected by the gas flow towards the gas outlet side. Subsequently,

the spatter particles fall down on the current powder bed layer. These agglomerated spatter would need far more laser energy to be entirely melted, which leads to an unmolten area without fusion (lack-of-fusion pores). The SLM 500 machine is equipped with four simultaneously running lasers. Each laser has its own working area. Apparently, an influence of different lasers was also detected. The area of laser 2 shows a highly increased amount of lack-of-fusion pores. On the other hand, the number of spherically shaped pores (most likely hydrogen-induced pores, especially class A) is decreased. The formation of various types of pores is highly depending on the volume energy input into the powder bed. The protective window of a laser can be contaminated by condensate and vapour plume from the melting process which causes a laser attenuation and

**Fig. 4** Pore classification results depending on the platform location



leads to an increased formation of lack-of-fusion pores. The more powder bed areas are exposed by the laser during the manufacturing process, the higher the contamination of the protective windows was. A few publications mention an influence of by-products on the laser powder bed fusion process [26–28]. Ladewig et al. [26] showed that locally different gas flow velocities are responsible for the insufficient removal of by-products originating from the manufacturing process. Typical by-products occurring during the laser powder bed fusion process can be welding plume (metal vapour or plasma plume), condensate, spatter or ejected powder [26]. The locally different pore type formation seems to be caused by an insufficient removal of process by-products. This assumption must be verified in further investigations. Nevertheless, using pore classification methods by means of X-ray data proves to be an appropriate tool to identify possible influences on the quality and helps to improve the AM process.

## 4 Conclusions

The used classification method for pores using X-ray data can provide a lot of precise information about the process conditions and the correlations between defects and LPBF process parameters. A total number of 2,939,830 pores in 96 cylindrical samples were detected and evaluated. On the one hand, the effect of various scanning speeds with and without prior in situ preparation of the powder was carried out. On the other hand, the reproducibility of the SLM 500 machine, as well as the influence of different lasers and the introduced shielding gas flow, was examined.

Several conclusions can be drawn from these studies:

- Using prior in situ laser powder preparation strategies (such as pre-sintering or pre-heating) reduces the total number of pores at high scanning speeds. When the scanning speed is increased, the number of spherically

shaped pores (most likely hydrogen and keyhole pores) usually decreases. Only the pre-heating process stopped the formation of spherical pores at a scanning speed of 1000 mm/s drastically.

- In general, the higher the introduced energy into the powder bed, the fewer irregularly shaped pores (classes D–F) and more spherical shaped pores (classes A–C) occurred.
- Pore classes E and F represent weak spots in an AM part and most often dictate the occurring component failure [11, 25]. Irregularly shaped pores (especially classes E and F) should be reduced by adapted process parameters or post-processing such as hot isostatic pressing.
- Condensate and vapour plume from the melting process could contaminate the protective window of a laser, which leads to the formation of lack-of-fusion pores. Furthermore, the shielding gas flow seems to stimulate the formation of lack-of-fusion pores (especially pore class D) at the gas outlet side due to weld spatter. The spatter leads to an insufficient energy input into the powder bed and hence to unmolten areas without fusion [4]. The locally different pore type formation seems to be caused by an insufficient removal of process by-products. A few publications mention an influence of by-products on the laser powder bed fusion process [26–28]. These assumptions must be verified in further investigations.

Even if the formation of pores cannot be completely suppressed, investigations using X-ray data prove to be an appropriate tool to determine the quality of AlSi10Mg parts [12–14]. Further investigations should be carried out using a multifactorial experimental design that allows finding significant interactions between different influences on the pore formation.

Nowadays, in situ process monitoring provides a lot of information about pore formation for each exposed layer. However, pores do not only appear on the top layers. Multiple layers are re-melted during the exposure and pores are created inside the component. Optical in situ monitoring does not provide enough information in this case. For today's high-tech applications in aerospace, medical, automotive and many more, quality assurance is more important than ever before. A consistent quality assurance including defect detection and process control is mandatory and can be carried out by means of X-ray data and suitable defect classification methods [11].

**Author contribution** Natan Nudelis was involved in conceptualization, methodology, data collection, data curation, formal analysis, visualization, investigation, validation, writing — original draft and writing — review and editing. The first draft of the manuscript was written by Natan Nudelis, and all authors commented on previous versions of the manuscript. All authors read and approved the final manuscript. Peter

Mayr helped in supervision, conceptualization and writing — review and editing.

**Funding** Open Access funding enabled and organized by Projekt DEAL.

**Data availability** Data are available on request.

**Code availability** Code is available on request.

## Declarations

**Ethics approval** Not applicable.

**Consent to participate** Not applicable.

**Consent for publication** Not applicable.

**Conflict of interest** The authors declare no competing interests.

**Open Access** This article is licensed under a Creative Commons Attribution 4.0 International License, which permits use, sharing, adaptation, distribution and reproduction in any medium or format, as long as you give appropriate credit to the original author(s) and the source, provide a link to the Creative Commons licence, and indicate if changes were made. The images or other third party material in this article are included in the article's Creative Commons licence, unless indicated otherwise in a credit line to the material. If material is not included in the article's Creative Commons licence and your intended use is not permitted by statutory regulation or exceeds the permitted use, you will need to obtain permission directly from the copyright holder. To view a copy of this licence, visit <http://creativecommons.org/licenses/by/4.0/>.

## References

1. Aboulkhair NT, Everitt NM, Ashcroft I, Tuck C (2014) Reducing porosity in AlSi10Mg parts processed by selective laser melting. *Addit Manuf* 1–4:77–86. <https://doi.org/10.1016/j.addma.2014.08.001>
2. Weingarten C, Buchbinder D, Pirch N, Meiners W, Wissenbach K, Poprawe R (2015) Formation and reduction of hydrogen porosity during selective laser melting of AlSi10Mg. *J Mater Process Technol* 221:112–120. <https://doi.org/10.1016/j.jmatprotec.2015.02.013>
3. King WE, Barth HD, Castillo VM, Gallegos GF, Gibbs JW, Hahn DE, Kamath C, Rubenchik AM (2014) Observation of keyhole-mode laser melting in laser powder-bed fusion additive manufacturing. *J Mater Process Technol* 214:2915–2925. <https://doi.org/10.1016/j.jmatprotec.2014.06.005>
4. Haeckel F, Meixlsperger M, Burkert T (2017) Technological challenges for automotive series production in laser beam melting. Proceedings of the 28th annual international Solid Freeform Fabrication Symposium. Austin, ATX, Texas. <https://doi.org/10.26153/tsw/16985>
5. Louvis E, Fox P, Sutcliffe CJ (2011) Selective laser melting of aluminium components. *J Mater Process Technol* 211:275–284. <https://doi.org/10.1016/j.jmatprotec.2010.09.019>
6. Read N, Wang W, Essa K, Attallah MM (2015) Selective laser melting of AlSi10Mg alloy: process optimisation and mechanical properties development. *Mater Des* 65:417–424. <https://doi.org/10.1016/j.matdes.2014.09.044>

7. Hasmuni N, Ibrahim M, Raus AA, Wahab MS, Kamarudin K (2018) Porosity effects of AlSi10Mg parts produced by selective laser melting. *J Eng Mech* 5(4):246–255
8. Ellendt N, Fabricius F, Toenjes A (2021) PoreAnalyzer—an open-source framework for analysis and classification of defects in additive manufacturing. *Appl Sci* 11:6086. <https://doi.org/10.3390/app11136086>
9. Leis A, Weber R, Graf T (2021) Process windows for highly efficient laser-based powder bed fusion of AlSi10Mg with reduced pore formation. *Materials* 14:5255. <https://doi.org/10.3390/ma14185255>
10. Trevisan F, Calignano F, Lorusso M, Pakkanen J, Aversa A, Ambrosio EP, Lombardi M, Fino P, Manfredi D (2017) On the selective laser melting (SLM) of the AlSi10Mg alloy: process, microstructure, and mechanical properties. *Materials* 10:76. <https://doi.org/10.3390/ma10010076>
11. Nudelis N, Mayr P (2021) A novel classification method for pores in laser powder bed fusion. *Metals* 11:1912. <https://doi.org/10.3390/met11121912>
12. Taute C, Möller H, du Plessis A, Tshibalanganda M, Leary M (2021) Characterization of additively manufactured AlSi10Mg cubes with different porosities. *J South Afr Inst Min Metall* 121:143–150. <https://doi.org/10.17159/2411-9717/1331/2021>
13. Cai X, Malcolm AA, Wong BS, Fan Z (2015) Measurement and characterization of porosity in aluminium selective laser melting parts using X-ray CT. *Virtual Phys Prototyp* 10:195–206. <https://doi.org/10.1080/17452759.2015.1112412>
14. Romano S, Abel A, Gumpinger J, Brandão AD, Beretta S (2019) Quality control of AlSi10Mg produced by SLM: metallography versus CT scans for critical defect size assessment. *Addit Manuf* 28:394–405. <https://doi.org/10.1016/j.addma.2019.05.017>
15. Ortega N, Martinez S, Cerrillo I, Lamikiz A, Ukar E (2017) Computed tomography approach to quality control of the Inconel 718 components obtained by additive manufacturing (SLM). *Procedia Manuf* 13:116–123. <https://doi.org/10.1016/j.promfg.2017.09.018>
16. du Plessis A, Yadroitsev I, Yadroitsava I, Le Roux SG (2018) X-ray microcomputed tomography in additive manufacturing: a review of the current technology and applications. *3D Print Addit Manuf* 5(3):227–247. <https://doi.org/10.1089/3dp.2018.0060>
17. Thompson A, Maskery I, Leach RK (2016) X-ray computed tomography for additive manufacturing: a review. *Meas Sci Technol* 27:072001. <https://doi.org/10.1088/0957-0233/27/7/072001>
18. Coro A, Macareno LM, Aguirrebeitia J, de Lacalle LNL (2019) A methodology to evaluate the reliability impact of the replacement of welded components by additive manufacturing spare parts. *Metals* 9:932. <https://doi.org/10.3390/met9090932>
19. Livings RA, Biedermann EJ, Wang C, Chung T, James S, Waller JM, Volk S, Krishnan A, Collins S (2020) Nondestructive evaluation of additive manufactured parts using process compensated resonance testing. In: Shamsaei N, Daniewicz S, Hrabe N, Beretta S, Waller J, Seifi M (eds) *Struct Integr Addit Manuf Parts*, PA: ASTM International, West Conshohocken, pp 165–205. <https://doi.org/10.1520/STP162020180111>
20. Slotwinski JA, Garboczi EJ, Stutzman PE, Ferraris CF, Watson SS, Peltz MA (2014) Characterization of metal powders used for additive manufacturing. *J Res Natl Inst Stand Technol* 119:460–493. <https://doi.org/10.6028/jres.119.018>
21. Dahmen T, Klingaa CG, Baier-Stegmaier S, Lapina A, Pedersen DB, Hattel JH (2020) Characterization of channels made by laser powder bed fusion and binder jetting using X-ray CT and image analysis. *Addit Manuf* 36:101445. <https://doi.org/10.1016/j.addma.2020.101445>
22. Ferro P, Meneghello R, Savio G, Berto F (2020) A modified volumetric energy density-based approach for porosity assessment in additive manufacturing process design. *J Adv Manuf Technol* 110:1911–1921. <https://doi.org/10.1007/s00170-020-05949-9>
23. Gu D, Yang Y, Xi L, Yang J, Xia M (2019) Laser absorption behavior of randomly packed powder-bed during selective laser melting of SiC and TiB2 reinforced Al matrix composites. *Opt Laser Technol* 119:105600. <https://doi.org/10.1016/j.optlastec.2019.105600>
24. Yang P, Deibler LA, Bradley DR, Stefan DK, Carroll JD (2018) Microstructure evolution and thermal properties of an additively manufactured, solution treatable AlSi10Mg part. *Mater* 33(23):4040–4052. <https://doi.org/10.1557/jmr.2018.405>
25. du Plessis A, Yadroitsava I, le Roux S, Yadroitsev I, Fieres J, Reinhart C, Rossouw P (2017) Prediction of mechanical performance of Ti6Al4V cast alloy based on microCT-based load simulation. *J Alloy Compd* 724:267–274. <https://doi.org/10.1016/j.jallcom.2017.06.320>
26. Ladewig A, Schlick G, Fisser M, Schulze V, Glatzel U (2016) Influence of the shielding gas flow on the removal of process by-products in the selective laser melting process. *Addit Manuf* 10:1–9. <https://doi.org/10.1016/j.addma.2016.01.004>
27. Shen H, Rometsch P, Wu X, Huang A (2020) Influence of gas flow speed on laser plume attenuation and powder bed particle pickup in laser powder bed fusion. *JOM* 72:1039–1051. <https://doi.org/10.1007/s11837-020-04020-y>
28. Santecchia E, Spigarelli S, Cabibbo M (2020) Material reuse in laser powder bed fusion: side effects of the laser - metal powder interaction. *Metals* 10(3):341. <https://doi.org/10.3390/met10030341>

**Publisher's note** Springer Nature remains neutral with regard to jurisdictional claims in published maps and institutional affiliations.